Design of Mixed-Matrix MOF Membranes with Asymmetric Filler Density and Intrinsic MOF/Polymer Compatibility for Enhanced Molecular Sieving

Rifan Hardian, Jiangtao Jia, Alejandro Diaz-Marquez, Supriyo Naskar, Dong Fan, Osama Shekhah, Guillaume Maurin, Mohamed Eddaoudi,* and Gyorgy Szekely*

The separation of high-value-added chemicals from organic solvents is important for many industries. Membrane-based nanofiltration offers a more energy-efficient separation than the conventional thermal processes. Conceivably, mixed-matrix membranes (MMMs), encompassing metal–organic frameworks (MOFs) as fillers, are poised to promote selective separation via molecular sieving, synergistically combining polymers flexibility and fine-tuned porosity of MOFs. Nevertheless, conventional direct mixing of MOFs with polymer solutions results in underutilization of the MOF fillers owing to their uniform cross-sectional distribution. Therefore, in this work, a multizoning technique is proposed to produce MMMs with an asymmetric-filler density, in which the MOF fillers are distributed only on the surface of the membrane, and a seamless interface at the nanoscale. The design strategy demonstrates five times higher MOF surface coverage, which results in a solvent permeance five times higher than that of conventional MMMs while maintaining high selectivity. Practically, MOFs are paired with polymers of similar chemical nature to enhance their adhesion without the need for surface modification. The approach offers permanently accessible MOF porosity, which translates to effective molecular sieving, as exemplified by the polybenzimidazole and Zr–BI–fcu-MOF system. The findings pave the way for the development of composite materials with a seamless interface.

1. Introduction

Chemical separation dominates the energy consumption of industrial processes.[1] In particular, various industries, including the petrochemical, pharmaceutical, fine chemical, food, and textile industries, use organic solvents extensively in their production.[2] Membrane-based processes have emerged as sustainable alternatives to distillation processes for the separation and purification of high-value-added chemicals and are expected to consume 90% less energy.[1] For efficient separation, the development of molecular sieving technologies with tunable properties (such as high selectivity, solvent resistance, mechanical stability, reproducibility, scalability, and economic feasibility) is of critical importance.

Metal–organic frameworks (MOFs) are a class of porous materials that are known for their ordered structures, adjustable porosity, and tunable functionality, and they have attracted widespread attention in many fields of applications, particularly for

R. Hardian, G. Szekely
Advanced Membranes & Porous Materials Center
Physical Sciences and Engineering Division (PSE)
Sustainable Separation Engineering Laboratory
King Abdullah University of Science and Technology (KAUST)
Thuwal 23955-6900, Saudi Arabia
E-mail: gyorgy.szekely@kaust.edu.sa

J. Jia, O. Shekhah, M. Eddaoudi
Advanced Membranes & Porous Materials Center
Physical Sciences and Engineering Division (PSE)
Functional Materials Design Discovery
and Development Laboratory (FMD3)
King Abdullah University of Science and Technology (KAUST)
Thuwal 23955-6900, Saudi Arabia
E-mail: mohamed.eddaoudi@kaust.edu.sa

A. Diaz-Marquez, S. Naskar, D. Fan, G. Maurin
ICGM
Univ. Montpellier
CNRS
ENSCM
Montpellier 34293, France

M. Eddaoudi
Chemical Science Program
Physical Science and Engineering Division (PSE)
King Abdullah University of Science and Technology (KAUST)
Thuwal 23955-6900, Saudi Arabia
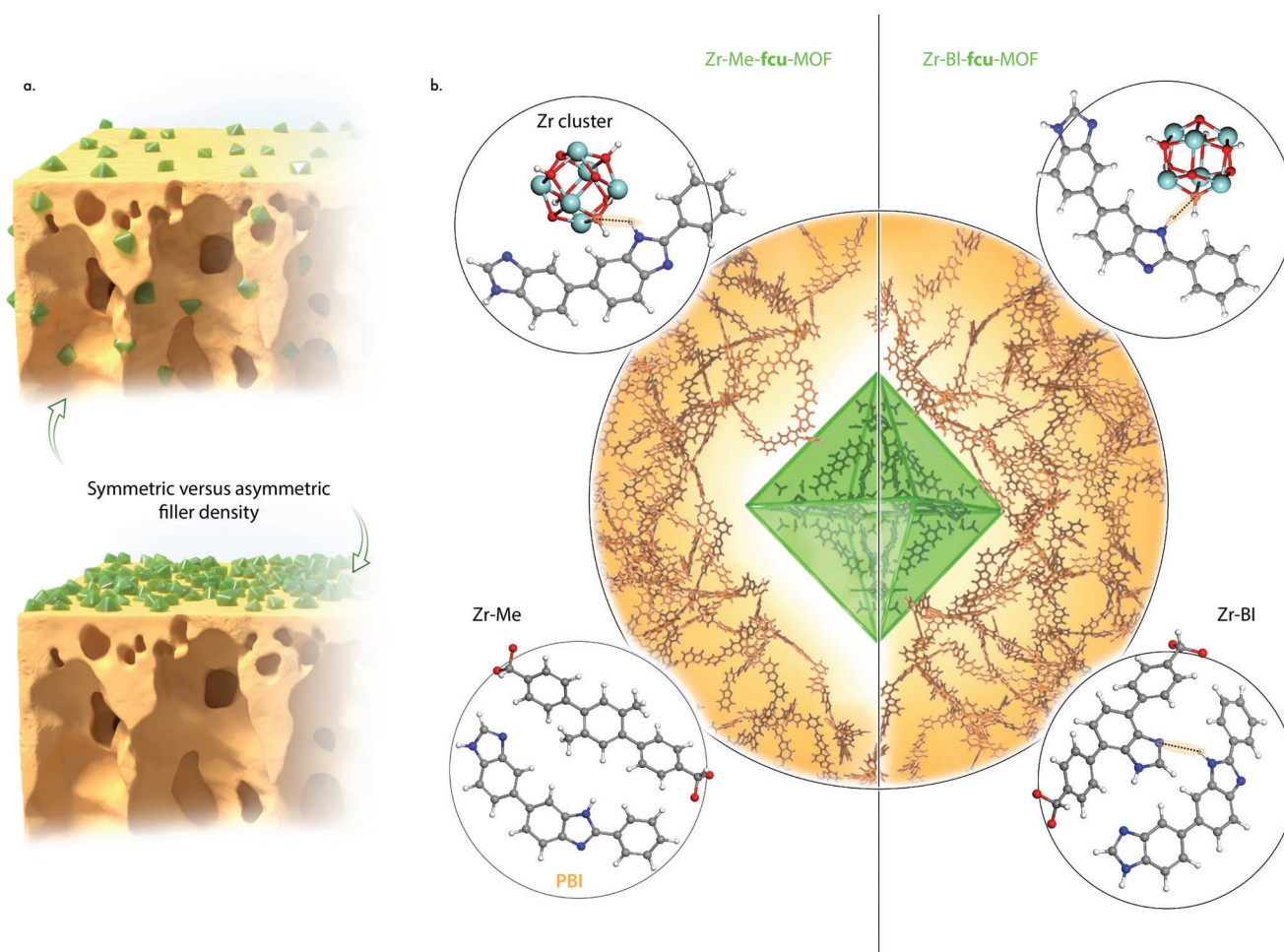
Figure 1. Design of MMMs. a) Schematic representation of the symmetric and asymmetric-MOF filler densities in MMMs resulting from the application of direct mixing or multizoning methods, respectively. When the MMM has a symmetric filler density, the MOF is evenly distributed throughout the cross-section of the membrane. When the MMM has an asymmetric filler density, the MOF is distributed only on the surface of the membrane. b) Illustration of the MOF–polymer interaction in two different systems: PBI with Zr–Me–**fcu**-MOF (M^{Me}) and PBI with Zr–BI–**fcu**-MOF (M^{BI}). Magnified illustrations highlight the interactions that govern MOF–polymer adhesion in the explored systems.

membrane separation.[3–5] In theory, the modularity of MOFs offers the ability to fine-tune their associated pore-apertures and in turn code their precise molecular sieving properties. However, pure MOF-based membranes are generally rigid,[6] which makes them fragile and difficult to scale up.[7] On the other hand, pure polymer membranes possess mechanical flexibility and processability, which makes them practically simple and facile to fabricate, scale up, and appropriate for various applications. Mixed-matrix membranes (MMMs), which comprise a polymer matrix and MOF fillers (**Figure 1**), enable a synergistic combination of the characteristics of both constituents.[8]

Because of its simplicity and rapid processing, phase inversion remains the most widely used technique for membrane

fabrication.[9] This technique involves the preparation of a dope solution, followed by casting and immersion in coagulation media. This typically generates an integrally skinned asymmetric (ISA) membrane with a unique structure: a thinner dense layer on top of a thicker sponge-like layer. The top layer controls selectivity, whereas the bottom layer provides mechanical support during filtration.

MMMs are mainly prepared by the direct mixing of a filler, such as MOFs, with a polymer solution, which results in the underutilization of the MOF fillers owing to their uniform distribution through the cross-section of the membrane. Consequently, most MOF nanoparticles are located inside the bulk part of the MMMs and not on their surface. Plausibly, the separation performance of the MMMs is influenced by the top layer of the membrane; therefore, most MOF nanoparticles do not contribute to the separation performance. The pore-aperture of MOFs influences the membrane's selectivity, whereas the amount of MOFs on the surface determines the solvent flux. Enhancing the separation performance of MMMs prepared using the direct mixing

G. Szekely
Chemical Engineering Program
Physical Science and Engineering Division (PSE)
King Abdullah University of Science and Technology (KAUST)
Thuwal 23955-6900, Saudi Arabia

method is often achieved by maximizing the MOF loading; however, this compromises the mechanical properties of the resulting membranes.[10] Therefore, concentrating the MOF nanoparticles on the membrane surface could minimize the need for high MOF loading, thereby achieving satisfactory separation performance while maintaining mechanical stability. Thus, innovative strategies for concentrating MOF nanoparticles on membrane surfaces are required.

The in-situ growth of MOFs in MMMs is a promising approach for maximizing the utilization of fillers.[11] However, the MOFs also grow throughout the cross-section of the membrane, thereby increasing the permeation path of the feed stream. Moreover, most reaction conditions required for MOF crystallization often involve harsh solvents, elevated temperatures, and relatively high pressure, which may lead to the degradation of the polymer matrix and ultimately limit the selection of MOF–polymer pairs. Thin-film nanocomposite (TFN) membranes, comprised of an ultrathin polyamide thin film embedded by porous fillers on top of a highly porous support, have attracted great interests owing to their high permeance. The in-situ formation of polyamide layer via interfacial polymerization required specific conditions (such as solvent systems) which could limit the selection of the monomers and their compatibility with MOFs.[12] An alternative method for better utilization of fillers in MMMs is the electrodeposition of MOFs on the surface of the polymer matrix.[13–15] However, electrodeposition requires i) solvents with specific electrolytic properties that enable MOF growth without deteriorating the polymer and ii) a conductive surface, which is a challenge in polymer matrices. In some cases, electrodeposition necessitates the use of a metal plate electrode as a metal source for MOF synthesis; however, a metal plate may be impractical and may limit the selection of MOFs to grow.[16] Moreover, in contrast to the direct mixing technique, in which the MOF nanoparticles are surrounded and embedded in the polymer matrix, the MOF–polymer adhesion in MMMs derived via electrodeposition may be weak because entanglement of the MOF and the polymer matrix is lacking.

Multilayer casting creates a thin layer of filler-containing dope solution on a membrane support to enable the distribution of fillers on the membrane surface.[17] However, an interface that reduces the adhesion between the layers is generated.[17–19] Such an interface undermines the mechanical stability of MMMs and may result in detachment or cracking of the layers. Herein, we propose circumventing this problem using an innovative multizoning method to cast the dope solution on top of a wet film instead of a membrane support (Figure S2, Supporting Information). We hypothesized that the multizoning method generates MMMs with asymmetric-filler density in a seamless interface-free polymer matrix in which the MOF fillers are distributed only on the surface of the membrane. Unlike the in-situ growth method, this method does not involve MOF crystallization, and therefore enables the independent optimization of the MOF and polymer matrix; thus, this method is applicable to a wide variety of MOF–polymer pairs.

Another important aspect of MMMs is the MOF–polymer adhesion. Incompatibility in MOF–polymer pairs may create interfacial voids that result in a preferential molecular path between the MOF and polymer which decreases the selectivity.[20] Several studies have reported strategies for improving this interfa-

cial adhesion, such as functionalizing either the polymer[21–23] or the surface of the MOFs[24–28] as well as creating MOF surface defects.[29] Here, we promoted adhesion by pairing an intrinsically compatible MOF and a polymer without the need for additional surface modification steps. The polybenzimidazole (PBI) polymer, which has been widely used for nanofiltration applications, is paired with a zirconium-based MOF with an underlying **fcu** topology, namely Zr–BI–**fcu**-MOF.[30] This MOF was constructed from the 12-connected hexanuclear zirconium cluster $[Zr_6(\mu_3\text{-}O)_4(\mu_3\text{-}OH)_4(O_2C-)_{12}]$, linked by the ditopic benzimidazole-functionalized ligand, deprotonated 4,4′-(1H-benzo[d]imidazole-4,7-diyl)dibenzoic acid. The Zr–BI–**fcu**-MOF encompasses tetrahedral and octahedral cages accessible solely through a triangular pore-aperture with a maximum opening of 0.85 nm (0.48–0.85 nm), suitable for separating organic molecules in nanofiltration applications. To elucidate the role of intrinsic chemical compatibility, imidazole moiety, with the polymer on nanofiltration applications, an isoreticular MOF, Zr–Me–**fcu**-MOF, was synthesized from the same zirconium cluster connected by a methyl-functionalized ligand, namely 2′,5′-dimethyl-[1,1′:4′,1′′-terphenyl]−4,4′′-dicarboxylate as a ligand, and paired with PBI.

A combined experimental and theoretical nanofiltration dataset was collected, and molecular modeling was performed to gain insight into the MMMs structure. Furthermore, the embedding of the MOF into the polymer matrix on the membrane surface was thoroughly investigated for the first-time using nano-Fourier transform infrared (nano-FTIR) spectroscopy to gain insights on the chemistry at the interface formed between the MOF and the polymer matrix at nanodomain. The stability of the MMMs in harsh organic solvents was enhanced using a one-pot crosslinking method for all the MMM constituents. We demonstrate an innovative multizoning technique for the design of optimum MMMs with an asymmetric-filler density and high compatibility between the MOF and polymer (Figure 1). This strategy is vital for fabricating MMMs with excellent solvent permeance and high selectivity.

2. Results and Discussion

2.1. Design of Asymmetric-Filler Density in MMMs

The rational design of MMMs was realized by pairing PBI with Zr–BI–**fcu**-MOF (M^{BI}) because of the similarity in their chemical moieties, i.e., the benzimidazole (BI) unit bearing interactive N—H groups. The application of the multizoning method concentrated the MOF distribution on the surface of the membrane. More details on the methodology are presented in the Experimental Section (Figure S2, Supporting Information), and the membrane designations are listed in Table S1 (Supporting Information). We specifically compared the multizoning method with direct mixing method for two main reasons: 1) direct mixing method is the most commonly used method in the fabrication of MMMs; 2) it is impossible to compare the performance of multizoning with multilayer membrane (which is fabricated by casting wet film on dry film), for the reason that the multilayer membrane is delaminated between the top zone and the bottom zone (Figure S9, Supporting Information). This delamination creates

**ADVANCED
SCIENCE NEWS**

www.advancedsciencenews.com

**ADVANCED
MATERIALS**

www.advmat.de
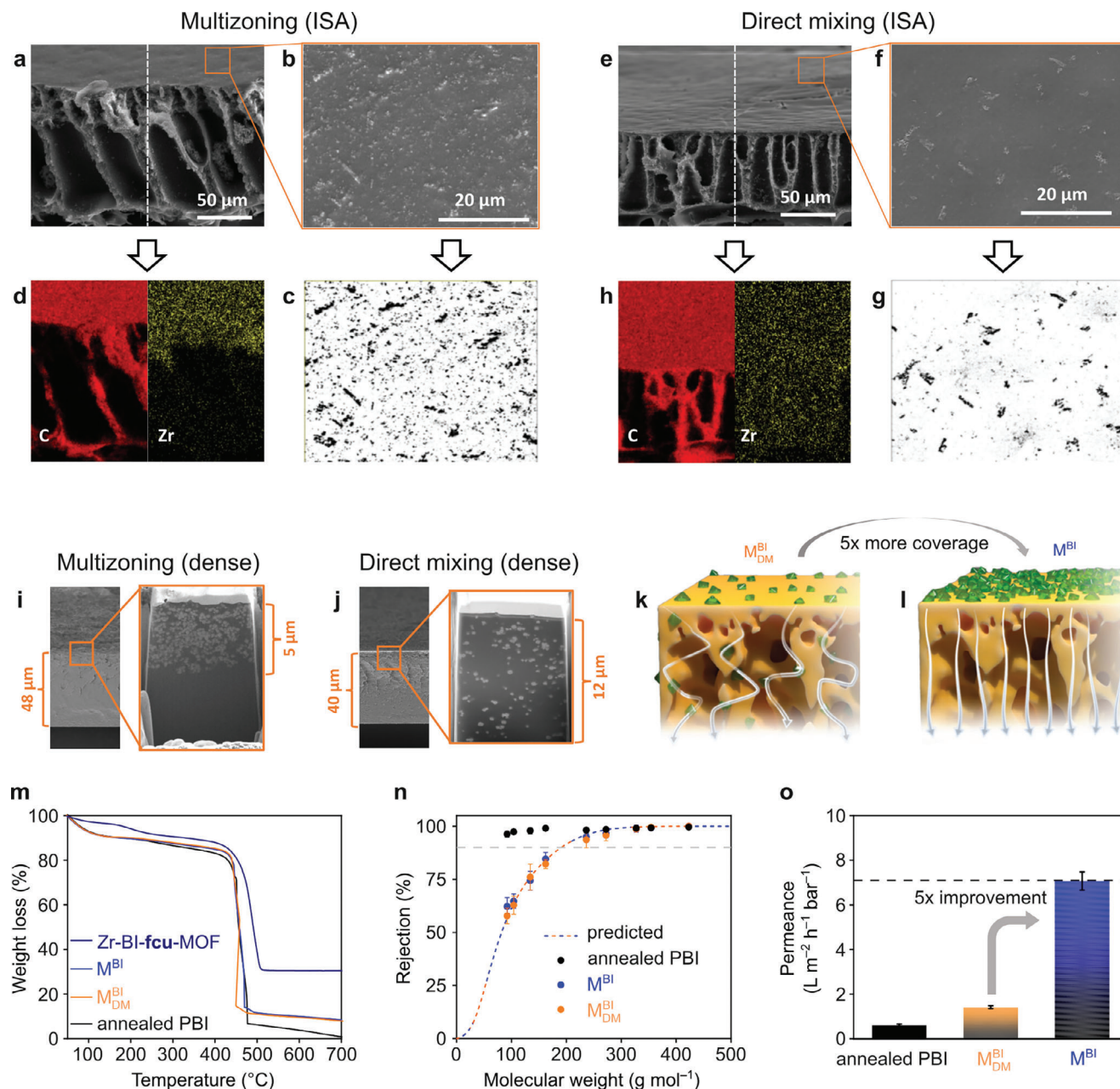
Figure 2. Filler distribution and transport pathway designs. Scanning electron microscopy (SEM) cross-section, surface, binary contrast, and cross-sectional EDX mapping images of M^{BI} prepared via multizoning a–d) and M_{DM}^{BI} prepared via direct mixing e–h) methods. Focused ion-beam scanning electron microscopy (FIB-SEM) cross-sectional images of dense membrane prepared via multizoning i) and direct mixing j). Proposed molecular transport pathways through M_{DM}^{BI} and M^{BI} k,l). TGA curves of Zr–BI–**fcu**-MOF, M^{BI}, M_{DM}^{BI}, and annealed PBI m). Rejection profile n) and acetone permeance o) of M^{BI} and M_{DM}^{BI}: the black solid and dashed lines in (n,o) indicate the predicted rejection and permeance values, respectively.

defects in the membrane that results in the membrane becoming not selective.

Using the dry weight PBI:MOF ratio of 90:10, as indicated by the thermogravimetric analysis (TGA) results (**Figure 2m**), the multizoning method (M^{BI}) produced a more homogenous surface coverage (Figure 2b,c) than the conventional direct mixing method, M_{DM}^{BI} (Figure 2f,g). TGA has been established as a reliable method to estimate the MOF content in mixed matrix membranes.[25,26,28,31,32] Markedly, due to the

multizoning method, most of the MOF nanoparticles are distributed at the surface of the membrane, whereas with the direct mixing method, most of the MOF nanoparticles are located at the cross-section (interior) of the MMMs. The energy dispersive -Xray (EDX) spectroscopy mapping of zirconium (representative of MOF nanoparticles) on the MMMs' cross-section confirmed the absence and presence of MOFs in the cross-section of M^{BI} (Figure 2d) and M_{DM}^{BI} (Figure 2h), respectively.

**ADVANCED
SCIENCE NEWS**

www.advancedsciencenews.com

**ADVANCED
MATERIALS**

www.advmat.de

Increasing the MOF loading cause difficulties during fabrication because the high MOF content significantly increases the viscosity of the dope solution, which cannot be cast into a film (Figure S4, Supporting Information). It is worth to mention that MOFs aggregation is not only influenced by the particle size,[33–36] but also by the dispersion media (concentration of the polymer solution). The multizoning method helps in minimizing the MOF dispersion issues through the multistep membrane fabrication protocol. The first step is to cast only the pure polymer solution with adequate viscosity at high concentration. The second step is to disperse the MOF nanoparticles in a dilute dope solution, followed by casting this solution on the freshly cast wet film.

Further investigation was carried out by preparing dense MMMs via both multizoning and direct mixing methods, followed by solvent evaporation. To obtain a clear image of the MOF distribution in the MMM cross-section, the membranes were cut and analyzed using a focused ion-beam scanning electron microscope (FIB-SEM). In the multizoning method, the MOFs nanoparticles were clearly observed only in the top zone at a penetration depth of ≈5 μm from the membrane thickness of ≈48 μm (Figure 2i). On the other hand, MOF nanoparticles were observed throughout the cross-section of the dense MMMs prepared via the direct mixing method (Figure 1j). These SEM observations showed that the multizoning method concentrates the MOF fillers on the surface of a membrane prepared via either phase inversion (ISA morphology) or solvent evaporation (dense morphology).

To ensure that molecular transport was mainly governed by the MOF porosity, the MMMs were annealed at 100 °C prior to the nanofiltration test. The curing process tightened the porosity of the polymer matrix and minimized the pathways for molecular transport through the polymer matrix. As seen in Figure 2n,o, the pristine annealed PBI membrane (without MOF) achieved a rejection of almost 100% for all small molecules (molecular weight as low as 100 g mol^{-1}) and showed negligible acetone permeance (0.61 ± 0.05 L m^{-2} h^{-1} bar^{-1}), which indicates the behavior of a nonporous membrane. Interestingly, both M^{BI} and M^{BI}_{DM} exhibited identical rejection curves that showed molecular weight cutoff (MWCO) values at 201 ± 19 and 203 ± 26 g mol^{-1}, respectively (Figure 2n). As shown in Figure 2o, the acetone permeance through M^{BI} (7.07 ± 0.41 L m^{-2} h^{-1} bar^{-1}) is almost five times higher than the acetone permeance through M^{BI}_{DM} (1.42 ± 0.06 L m^{-2} h^{-1} bar^{-1}). Because the rejection curves of M^{BI} and M^{BI}_{DM} are identical, the lower solvent permeance in M^{BI}_{DM} can be attributed to the presence of a lower MOF content on the membrane surface, which provides fewer channels for facilitating solvent transport. The transport pathways of the solvent through M^{BI}_{DM} and M^{BI}_{DM} are illustrated in Figure 2k,l, where the presence of a greater number of MOF nanoparticles on the membrane surface resulted in a higher flux. With the same amount of MOF loading, the MOF nanoparticles covered almost 50% of the M^{BI} surface (Figure 2c), whereas they covered only ≈10% of the M^{BI}_{DM} surface (Figure 2g). The MOF coverage on the membrane surface was estimated from the scanning electron microscopy (SEM) images using imaging software (imageJ) and color contrast, where black and white regions represent the MOF nanoparticles and the polymer matrix, respectively. The differences in MOF coverage were correlated with the difference in solvent permeances,

where M^{BI} demonstrated a permeance that was approximately five times higher than that of M^{BI}_{DM}.

Moreover, both the experimental MWCO and solvent permeance values of M^{BI} matched well with the predicted MWCO and solvent permeance values (191 g mol^{-1} and 7.10 L m^{-2} h^{-1} bar^{-1}, respectively), as shown in Figure 2n,o, which suggests that the presence of MOFs provided channels for molecular transport. In contrast, the solvent permeance through M^{BI}_{DM} was approximately five times lower than the predicted value, indicating a limited molecular transport through the membrane. The predicted MWCO and permeance values were calculated by applying the pore flow model, considering the largest possible pore-aperture of the Zr–BI–**fcu**-MOF (0.85 nm) and assuming a laminar solution flux through the cylindrical pore channels perpendicular to the plane of the membrane. A more detailed explanation of the pore flow model is provided in the Supporting Information.

To evaluate the mechanical stability of the membranes in real applications, M^{BI} was tested at various applied pressures during nanofiltration experiment (Figure S14, Supporting Information). The solvent flux linearly increased with the increase in pressure, which indicates that the membrane could withstand high pressure (tested up to 50 bar), testifying its mechanical stability. The linear relationship suggests that there is no membrane compaction under the applied conditions.

In addition, the phenomenon of MOF embedment by the polymer matrix on the membrane surface was investigated in-depth using nano-FTIR spectroscopy. Standard attenuated total reflectance (ATR)-FTIR spectroscopy is constrained by a large scanning size (micrometer) that provides low spatial resolution and it is not equipped with a high-resolution microscope for selecting the location of the FTIR collection. Thus, the ATR-FTIR spectroscopy generates average chemical information for the MMMs by combining the spectra of both MOF and polymer matrix. In contrast, combined atomic force microscope (AFM) and FTIR in nano-FTIR spectroscopy allowed us to identify the chemical variability in the nanodomain (in this case, with a spatial resolution of 30 nm).[37] The nano-FTIR spectroscope was equipped with a very sharp probe (AFM tip with a diameter of ≈2–5 nm) and a high-resolution microscope, which enabled us to locate the MOF nanoparticles on the MMM surface and separately measure the spectra of the MOF and polymer on the MMM surface.

The agglomerated MOF particles on the M^{Me} surface exhibited lateral dimensions and height of ≈6 and 1.5 μm, respectively (**Figure 3a**). A 3D topographical image is shown in Figure 3b, where black line marked locations for nano-FTIR line scanning. A 2D representation of the nano-FTIR spectra along the black line in Figure 3b is presented in Figure 3c. From this line scanning, a spectral change was observed, as indicated by a decrease in some characteristic peaks of PBI (in-plane deformation of the benzimidazole ring at a wavenumber of ≈1450 cm^{-1}) accompanied by the appearance of a new peak that is characteristic of the carboxylate group in the MOF (at a wavenumber of ≈1413 cm^{-1}). On the surface of the MOF agglomerate, only the FTIR peak corresponding to the MOF was observed, whereas no FTIR peak of the polymer was detected. These observations indicated that on the surface of the MMMs, the MOF nanoparticles were partially covered by the polymer matrix and other parts protruded from the membrane surface, as illustrated in Figure 3d. This finding is the first

ADVANCED
SCIENCE NEWS

www.advancedsciencenews.com

ADVANCED
MATERIALS

www.advmat.de
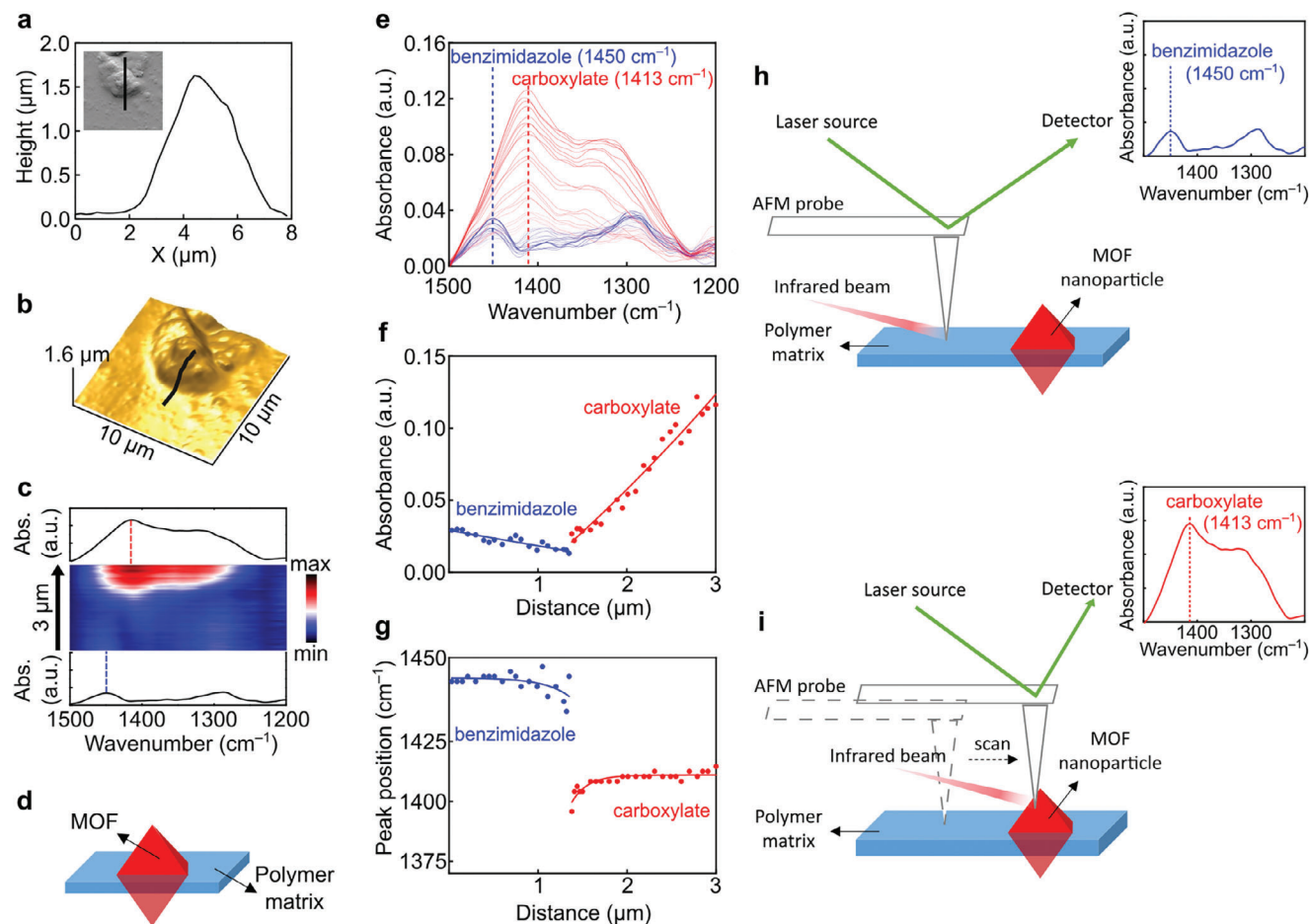
Figure 3. Nanodomain analysis of MOF embedment on MMM surface. The dimension of a MOF agglomerate in the polymer matrix; inset is the AFM height profile a). AFM 3D topography image of (a); black line indicates the nano-FTIR line scan b). 2D representation of the nano-FTIR spectra along the black line in (b) c). Illustration of MOF nanoparticles on the membrane surface partially covered by polymer matrix d). Nano-FTIR spectra along the black line in (b) with a spatial resolution of 30 nm e). Nano-FTIR absorbance f) and peak position g) along the black line in (b). Schematic representation of the processes used to acquire the nano-FTIR spectra of a polymer matrix h) and MOF nanoparticles i). All the data in 3 were obtained from sample M^{Me}.

direct observation that the polymer does not fully cover the MOF on the MMM surface, which is relevant for confirming the transport mechanism through MOF porosities. Although the MMMs were annealed to close the polymer pores, molecular transport still occurred through the MOF pores, because the MOF surface was not fully covered by the polymer. These hypotheses were supported by the nanofiltration experiments (Figure 2n,o), where the annealed pristine PBI membrane exhibited almost no solvent flux and rejected all the tested solutes, while the MMMs demonstrated selective separation according to the pore-aperture size of the MOFs.

The evolution of the nano-FTIR spectra along the scanning line was also presented in Figure 3e, where the polymer peak diminished and the MOF peak gradually increased, and reaching an absorbance intensity that was three times higher than the absorbance of the polymer matrix. Further analysis was performed by quantifying the nano-FTIR absorbance intensity (Figure 3f) and peak positions (Figure 3g). The nano-FTIR absorption was deflected at ≈1.3 μm in the line scan, and the signal increased dramatically corresponding to the exposure of MOF particles

to the infrared beam. Schematic illustrations are presented in Figure 3h,i to describe the process of acquiring the nano-FTIR spectra of the polymer matrix and the MOF nanoparticles on the MMM surface, and Video S1 is included in the Supporting Information. Additionally, we also performed nano-FTIR analysis on M^{BI}, which consists of polybenzimidazole matrix and Zr–BI–**fcu**-MOF nanoparticles. Both the polymer matrix and the nanoparticles contain imidazole unit; however, carboxylate moieties are only present in the MOF structure (Figure S12, Supporting Information). Alternatively, we can clearly distinguish the regions of the MOF, the interface, and the polymer matrix by focusing on the evolution of the carboxylate peak.

2.2. MOF Chemistries in MMMs, and their Nanofiltration Performance

To investigate the effect of MOF linkers on nanofiltration performance, we compared two MMMs fabricated via the multizoning method by combining PBI with MOFs: Zr–BI–**fcu**-MOF

**ADVANCED
SCIENCE NEWS**

www.advancedsciencenews.com

**ADVANCED
MATERIALS**

www.advmat.de
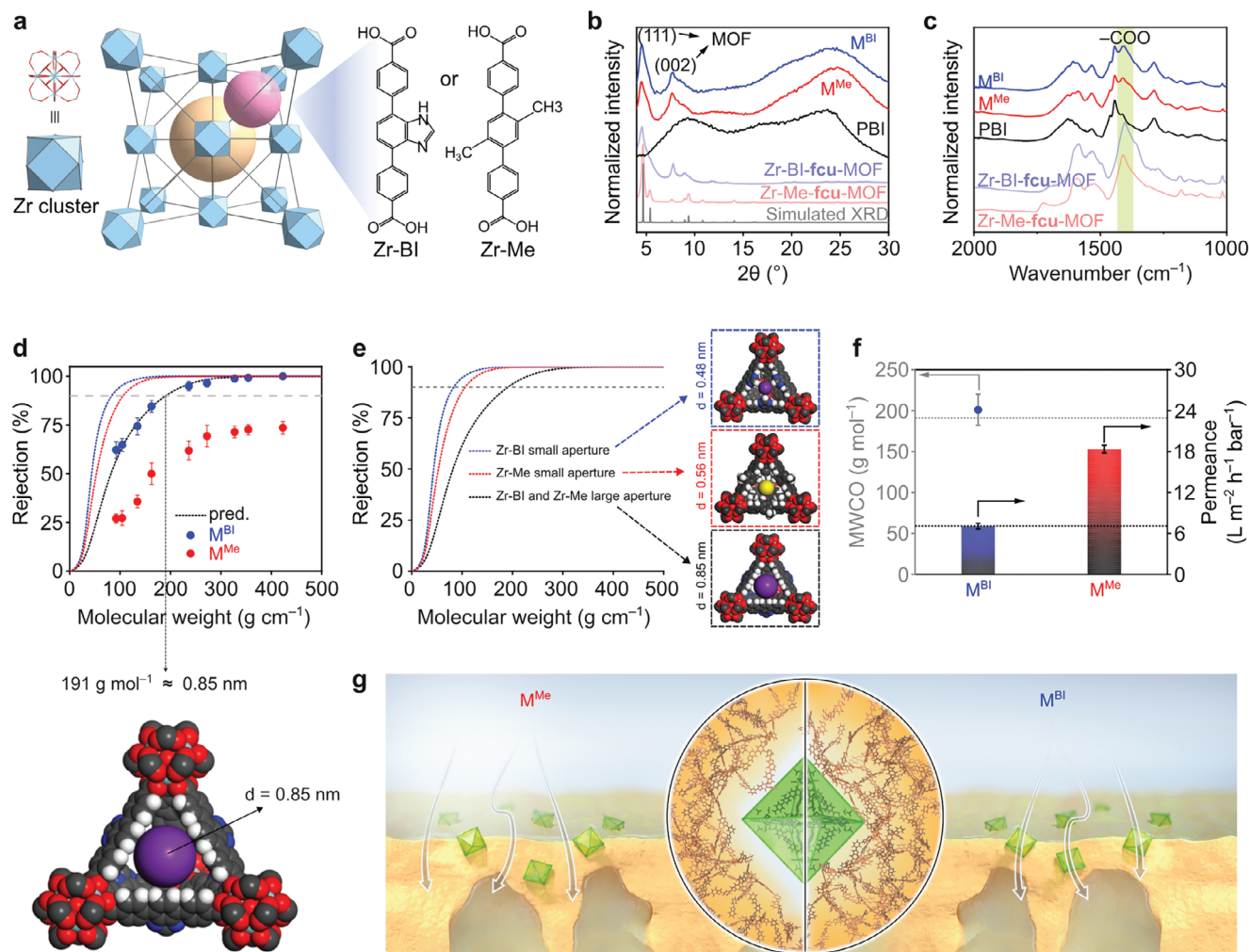
Figure 4. MOF design for molecular sieving in organic solvents. Structural representation of Zr-**fcu**-MOF with imidazole or methyl functionalization a). XRD b) and FTIR c) spectra of Zr–BI–**fcu**-MOF, Zr–Me–**fcu**-MOF, pristine PBI membrane, M^{BI}, and M^{Me}. d) Solute rejection curves of M^{BI} and M^{Me}; circles represent the experimental values. The dotted blue line represents the predictive rejection curves for the tightest possible pore apertures of Zr–BI–**fcu**-MOF. The dotted red line represents the predictive rejection curves for the tightest possible pore apertures of Zr–Me–**fcu**-MOF. The dotted black line represents the predictive rejection curves for the largest possible pore apertures of both Zr–BI–**fcu**-MOF and Zr–Me–**fcu**-MOF. The gray dashed line indicates a 90% rejection for estimating the MWCO values. e) Predictive rejection curves for the tightest and largest possible pore apertures of Zr–BI–**fcu**-MOF and Zr–Me–**fcu**-MOF along with their corresponding pore geometries. f) Acetone permeance through M^{BI} and M^{Me} (bar graph) and experimental MWCO values (circle). The gray and black dashed lines in (f) indicate the predicted MWCO and acetone permeance values, respectively. g) Schematic illustration of the possible molecular transport with molecules transported through interfacial voids for M^{Me}, and through MOF pores for M^{BI}.

containing benzimidazole-functionalized linker (M^{BI}) and Zr–Me–**fcu**-MOF containing dimethyl-functionalized linker (M^{Me}). The structures of these MOFs are shown in **Figure 4a**. Both MOFs exhibit an underlying **fcu** topology with tetrahedral and octahedral cages. The X-ray diffraction (XRD) patterns of both Zr–BI–**fcu**-MOF and Zr–Me–**fcu**-MOF (Figure 4b) confirmed their structures, as evidenced by matching the XRD patterns with the simulated XRD patterns. The XRD pattern of the pristine PBI polymer membrane showed a typical amorphous characteristic with a broad hump at 2θ of ≈25°.[38] The appearance of distinct XRD peaks in both M^{BI} and M^{Me} at 2θ ≈4.7° and ≈7.8° (corresponding to the (111) and (002) planes, respectively, of the **fcu** MOFs) indicated the persistence of MOF crystallinity in both MMM systems. The reason that the XRD peaks are broader in the case of

Zr–BI–**fcu**-MOF as compared to Zr–Me–**fcu**-MOF can be associated with their smaller particle size (41 nm) compared to the size of Zr–Me–**fcu**-MOF (69 nm), as shown in the SEM images (Figure S5, Supporting Information).

The presence of MOFs in the MMMs was also characterized by ATR-FTIR, with a band centered at ≈1413 cm^{-1}, which is characteristic of the carboxylate function of the MOFs (Figure 4c). Both MMMs were thermally stable, and their degradation began at ≈400 °C (Figure S13, Supporting Information). In situ TG-FTIR analysis revealed that weakly-bonded water molecules adsorbed on the membrane surface were released when MMMs were heated to 400 °C, as indicated by the strong peaks between 1200–1800 and 3500–3800 cm^{-1} (Figure S13, Supporting Information). A more strongly-bonded hydroxyl group (at 3200 cm^{-1}),

which could be originated from the MOF structure, started to be released at 250 °C. At temperatures above 400 °C, ammonia began to evolve (observed at 950 cm^{-1}), which could have been caused by decomposition of the imidazole unit in the polymer matrix.

Owing to the possible rotation of the linkers, both MOFs can exhibit dynamic pore apertures, where the smallest possible pore apertures for Zr–BI–**fcu**-MOF and Zr–Me–**fcu**-MOF are 0.48 and 0.56 nm, respectively, and the largest possible pore-aperture size for either MOF is 0.85 nm (Figure 4e). We used the pore flow model to develop predictive rejection curves from different possible scenarios for the MOF pore apertures (Figure 4e). The predictive rejection curves for the smallest apertures of the Zr–BI–**fcu**-MOF and Zr–Me–**fcu**-MOF are shown in blue and red dotted lines, respectively, whereas the predictive rejection curve from the MOFs having the largest apertures is shown by a black dotted line. The experimental rejection profile of M^{BI} demonstrated a good fit with its theoretical prediction when the largest MOF pore aperture size was used, with rejection reaching 100% for solutes larger than 350 g mol^{-1} (Figure 4d). The excellent fit between the experimental and predictive rejection curves confirmed that molecular transport occurred through the ordered porous structure of the MOFs, and suggested that there were no interfacial voids (defects) present between the MOFs and the polymer matrix. On the other hand, the rejection profile of M^{Me} deviated from the theoretical data and exhibited considerably lower rejection values across the nanofiltration range and culminated at the highest solute rejection values of ≈75%. Furthermore, the experimental 18.3 ± 0.5 L m^{-2} h^{-1} bar^{-1} acetone permeance through M^{Me} was found to be more than twice as high as the corresponding 7.1 ± 0.4 L m^{-2} h^{-1} bar^{-1} value for M^{BI}. The loss of selectivity associated with the increase in permeability suggests that the Zr–Me–**fcu**-MOF nanoparticles and PBI matrix are incompatible under the harsh conditions imposed by organic solvent nanofiltration. These conditions, i.e., high pressure and polar solvents, may have created nonselective interfacial voids and enabled solute molecules of different sizes (molecular weight from 100 to 450 g mol^{-1}) to pass through the membrane (Figure 4g).
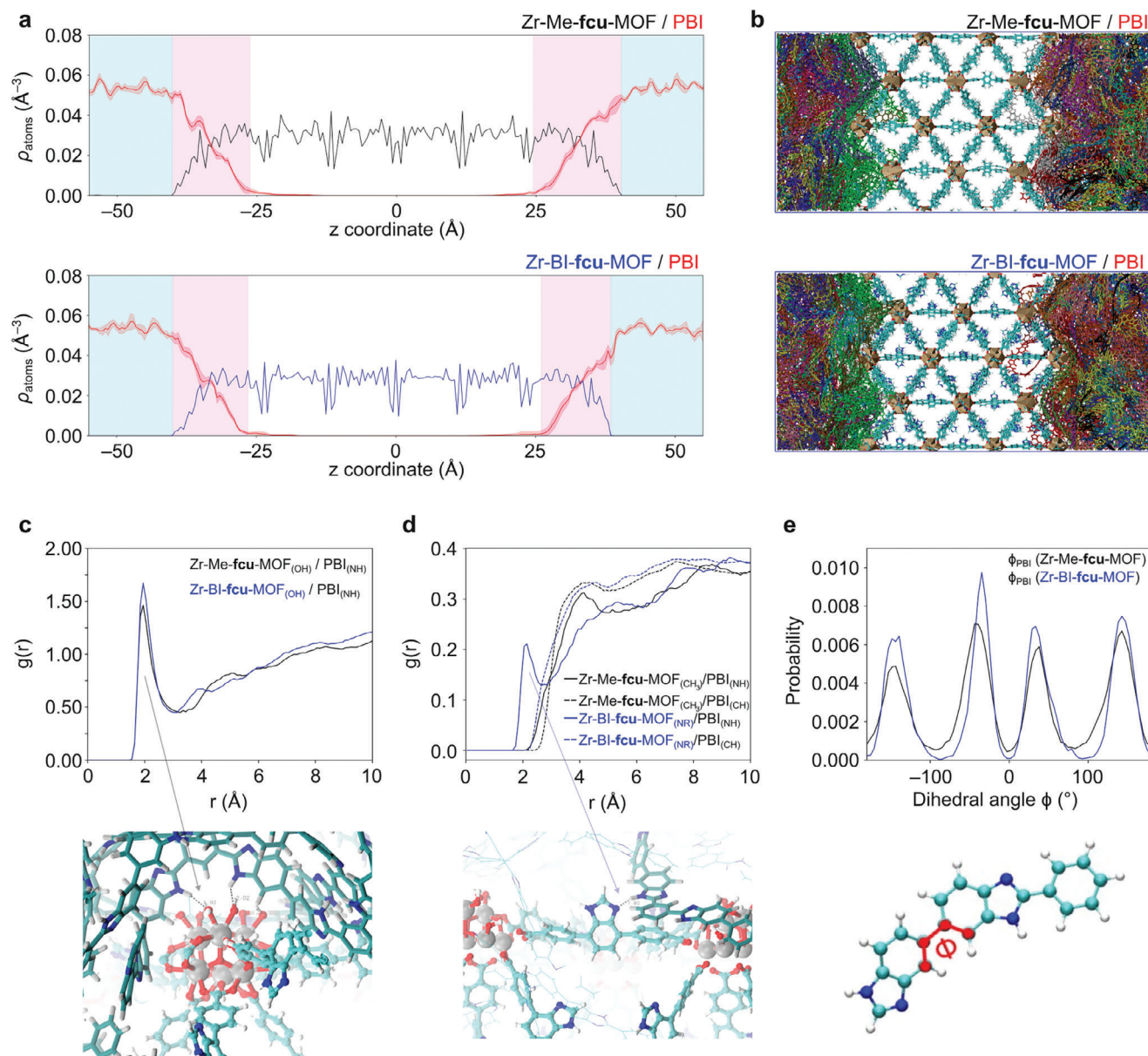
The presence of micrometer-size interfacial defects between the MOF and the polymer was observed by SEM,[24] but nanometer-size interfacial defects cannot be detected. Therefore, we indirectly evaluated the nanometer-size defects by performing nanofiltration experimentally, and compared the results with predictions based on the pore-flow model. Although the SEM images of both Zr–BI–**fcu**-MOF and Zr–Me–**fcu**-MOF exhibited seemingly good adhesion with the polymer (Figure S6, Supporting Information), the nanofiltration results of M^{Me} showed a large deviation from the expected results. This indicated the presence of defects that were larger than the pore size of the MOF.

To gain microscopic insight into the nanostructuring of the MOF–polymer interfaces in both MMMs, we deployed a modeling approach that integrates quantum calculations and force-field molecular dynamics (MD) simulations.[32,39] Atomistic models for both M^{BI} and M^{Me} were constructed by assembling i) the representative (110) MOF surface slabs with their exposed triangular pore apertures cleaved from the crystal structures of both MOFs,

which were preliminarily geometrically optimized at the density-functional theory (DFT) level, and ii) a 3D-structure model of the PBI polymer constructed by force-field-MD simulations as implemented in Polymatic code,[40] with an associated density of 1.11 g cm^{-3} that matches well with the experimental value of the bulk polymer.[38] The resulting MOF–PBI models were further equilibrated by means of a series of forcefield-based NVT and NPT MD runs using the LAMMPS code.[41] The force-field parameters and MD simulation settings are provided in the Supporting Information. The atomic density profiles for the MOF–PBI models are plotted along the z-direction normal to the MOF surface, with the MOF slab models located in the middle of the simulation box and surrounded by the PBI polymer (**Figure 5**a). The atomic density of PBI oscillates around a mean value far from the MOF surfaces, and it decays to zero in close proximity. One can observe that M^{BI} and M^{Me} show a similar MOF–polymer overlap length about of 1.4 ± 0.1 nm (pink zone), evaluated as the distance between the z value for which the MOF atomic density becomes zero and the z value for which the PBI atomic density tends to zero. This result indicates that there is an equivalent penetration of PBI into the first cavities of both MOFs closest to their external surfaces in both composites, as depicted by the illustrative representations of the atomistic models for M^{Me} (top) and M^{BI} (bottom) (Figure 5b). This partial polymer infiltration occurs throughout the exposed triangular windows of the MOFs that are large enough to accommodate the insertion of PBI moiety.

The comparison of the pore limiting diameters (PLD) for Zr–Me–**fcu**-MOF and Zr–BI–**fcu**-MOF indicates that they have similar triangular aperture sizes, (see details in the Supporting Information), allowing equivalent polymer penetration in M^{Me} and M^{BI}. Notably, such polymer penetration might suggest partial blockage of the MOF pores for the passage of solute/solvent molecules. This motivated us to identify the resulting interactions between PBI and the internal pore walls of the MOFs. Analysis of the radial distribution functions (RDF) of different MOF–PBI atom pairs showed that the hydroxyl functions of both MOFs interact predominantly with the —NH group of PBI$_{NH}$, with an associated separating distance of 0.195 nm (Figure 5c). Figure 5d reveals that there are relatively strong additional interactions between PBI and the imidazole groups of Zr–BI–**fcu**-MOF (main peak at 0.205 nm), whereas PBI interact weakly with the methyl groups of Zr–Me–**fcu**-MOF (mean peak at 0.40 nm). We performed additional DFT simulations on model clusters to estimate the interaction energy between each MOF and PBI and these calculations confirmed that Zr–BI–**fcu**-MOF interacts more strongly with PBI than does Zr–Me–**fcu**-MOF (see details in the Supporting Information). These overall predictions suggest that PBI is better stabilized in the pores of Zr–BI–**fcu**-MOF and hence less mobile, which prevents complete obstruction of the MOF cavities. Figure 5e also shows that PBI exhibits a narrower averaged dihedral angle distribution for M^{BI} versus M^{Me}, which implies that the polymer dynamics in the Zr–BI–**fcu**-MOF is much more restricted, consistent with the stronger PBI and Zr–BI–**fcu**-MOF interactions, as evidenced from the RDF plots. These observations provide evidence of a tighter control of the accessible MOF pore dimensions in M^{BI} versus M^{Me} in line with a better rejection performance of M^{BI} compared to that of M^{Me}.

**ADVANCED
SCIENCE NEWS**

www.advancedsciencenews.com

**ADVANCED
MATERIALS**

www.advmat.de

Figure 5. Nanostructuring of the MOF–polymer interfaces in M^{BI}, and M^{Me}. a) Atomic density profiles of PBI (red line), Zr–Me–**fcu**-MOF (black line), and Zr–BI–**fcu**-MOF (blue line) in M^{Me} (top) and M^{BI} (bottom), plotted along the z-direction normal to the MOF surfaces. b) Representative illustrations of the M^{Me} (top) and M^{BI} (bottom) membranes, PBI colored by chains. Radial Distribution Functions for the pairs c) Zr-Me-**fcu**-MOF$_{(OH)}$/PBI$_{(NH)}$ (black line) and Zr–BI–**fcu**-MOF$_{(OH)}$/PBI$_{(NH)}$ (blue line) and d) $Zr-Me-fcu-MOF_{(CH_3)}$/PBI$_{(NH)}$ (black line), $Zr-Me-fcu-MOF_{(CH_3)}$/PBI$_{(CH)}$ (black dashed line), Zr–BI– –**fcu**-MOF$_{(NR)}$/PBI$_{(NH)}$ (blue line), and Zr–Me-**fcu**-MOF$_{(NR)}$/PBI$_{(CH)}$ (blue dashed line). e) PBI dihedral angle distribution of representative angle (Φ), M^{Me} (black line), and M^{BI} (blue line).

2.3. Crosslinking MMMs with Distinct MOF Chemistry

Dibromo-xylene (DBX) has commonly been used as a crosslinker agent to improve the solvent stability of various polymer systems.[42,43] The stability of MMMs in organic solvent was tested by immersing them in dimethylacetamide (DMAc) (**Figure 6a**). Before crosslinking with DBX, both M^{BI} and M^{Me} dissolved rapidly in DMAc within 5 min of soaking. After the crosslinking, both MMMs (denoted as M_C^{BI} and M_C^{Me}) exhibited excellent solvent-resistant properties without any dissolution. The pro-

posed crosslinking mechanism for PBI–PBI and PBI–MOF is schematically presented in Figure 6b. In the case of M_C^{BI}, DBX facilitated crosslinking by connecting the nitrogen atoms in the PBI backbones with the nitrogen atoms from the imidazole in the Zr–BI–**fcu**-MOF. In the case of M_C^{Me}, only the nitrogen atoms in the PBI backbones were crosslinked by DBX, whereas the Zr–Me–**fcu**-MOF linker was not crosslinked via DBX.

The presence of a crosslinker in both M_C^{BI} and M_C^{Me} was evidenced by their characteristic ATR-FTIR spectra (Figure 6c) at 2918 and 2849 cm^{-1}, which were attributed to C—H (the terminal
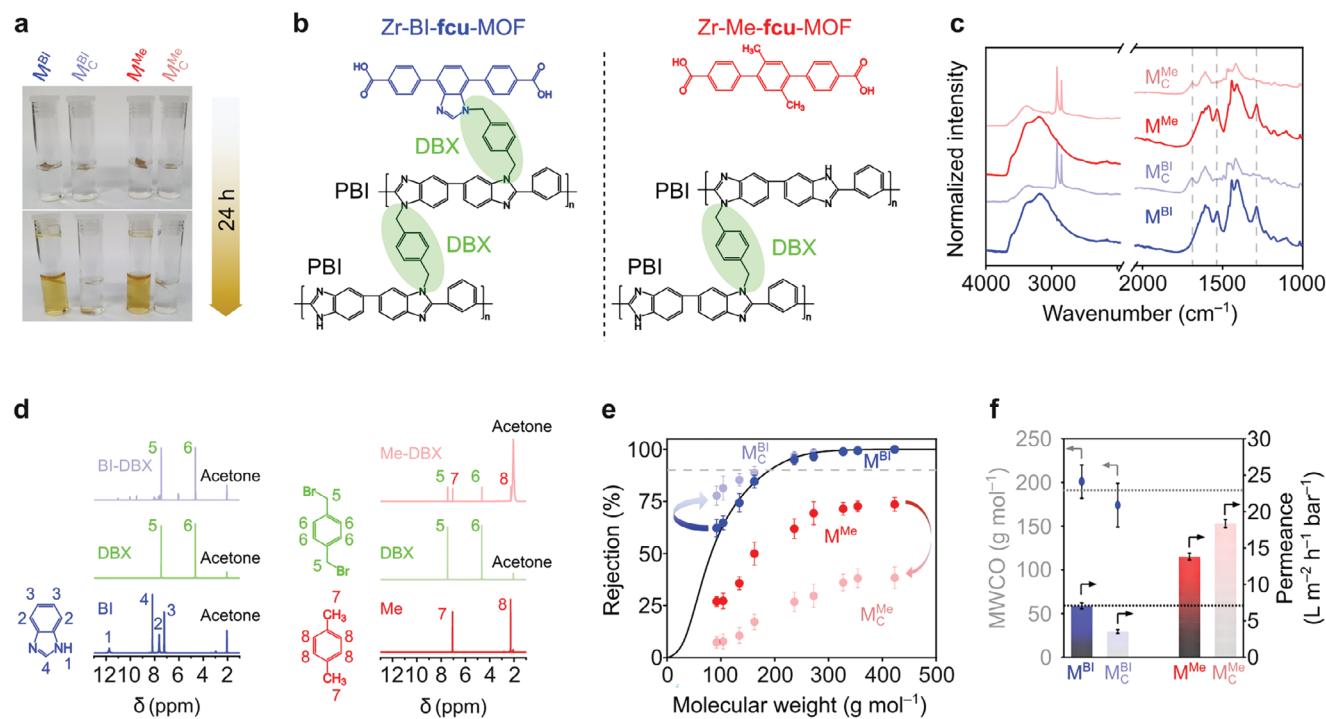
Figure 6. Crosslinking MMMs with distinct MOF chemistry. Solvent stability test of MMMs before (M^{BI} and M^{Me}) and after (M_C^{BI} and M_C^{Me}) crosslinking; solvent stability test was performed in DMAC solvent a). Proposed crosslinking mechanism in M_C^{BI} and M_C^{Me} b). FTIR spectra of the MMMs before (M^{BI} and M^{Me}) and after (M_C^{BI} and M_C^{Me}) crosslinking c). ^{1}H NMR spectra of benzimidazole (BI) and p-xylene (Me) before and after the reaction with the DBX crosslinker d). Solute rejection curves before (M^{BI} and M^{Me}) and after (M_C^{BI} and M_C^{Me}) crosslinking: The solid line represents the predictive values, and circles represent the experimental values e). MWCO values (circles) and acetone permeance through the MMMs (bar graph): Gray and black dashed lines indicate the predicted MWCO and permeance values f).

C of the crosslinker) and C—N (the link between the crosslinker and the polymer backbone) stretching.[42] Nevertheless, the ATR-FTIR spectra could not rule out whether crosslinking occurred only in the PBI matrix or if it involved the MOF linkers. To further investigate the possible crosslinking reaction that could involve the MOF linkers, a model reaction between benzimidazole (to mimic the linker in Zr–BI–**fcu**-MOF) and DBX was studied using liquid nuclear magnetic resonance (NMR) spectroscopy. The ^{1}H NMR spectra revealed that the characteristic chemical shift of benzimidazole (BI) disappeared after crosslinking with DBX (Figure 6d). Moreover, several new peaks appeared after the reaction between benzimidazole and DBX, suggesting that other complex reaction products had formed. These observations confirmed the occurrence of a reaction between the Zr–BI–**fcu**-MOF linkers and DBX. Furthermore, a model reaction between p-xylene (to mimic the Zr–Me–**fcu**-MOF linker) and DBX was also investigated. Interestingly, ^{1}H NMR spectra showed that no reaction occurred between p-xylene and DBX. The peaks of the individual precursors (p-xylene and DBX) remained the same after the crosslinking reaction was performed, and no new peaks were observed. These model reaction investigations revealed that DBX only crosslinked the linker of Zr–BI–**fcu**-MOF and not that of Zr–Me–**fcu**-MOF.

Furthermore, a nanofiltration experiment was performed to evaluate the effect of crosslinking on the molecular sieving properties of the two MMMs. The solute rejection data for M^{BI} followed the predicted rejection curve (Figure 6e), and a negligible

shift to a slightly higher rejection profile was observed for M_C^{BI}, indicating the effect of crosslinking on tightening the pores of the MMMs. We hypothesized that crosslinking both the polymer and MOFs further improved the MOF–polymer adhesion, thereby generating slightly tighter pores. The corresponding MWCO values for M^{BI} and M_C^{BI} were 201 ± 17 and 174 ± 25 g mol^{-1}, respectively. Pore tightening was also reflected by the lower acetone permeance of the M_C^{BI} compared to M^{BI} (Figure 6f). In the case of M^{Me}, as explained earlier, the rejection data deviated from the prediction data with a significantly lower rejection profile (less than 90%), which is indicative of a nonselective membrane due to the formation of interfacial voids. In the previous section, we proved that the interfacial voids in M^{Me} were caused by the low compatibility between the Zr–Me–**fcu**-MOF linker and the PBI polymer matrix. Moreover, the rejection curve of M_C^{Me} was even lower than that of M^{Me}, suggesting the formation of defective MMMs that created even larger interfacial voids. We assume that the lower compatibility between the Zr–Me–**fcu**-MOF linker and the PBI matrix, along with the nonreactivity of the Zr–Me–**fcu**-MOF linker toward the DBX crosslinker, worsens the MOF–polymer adhesion and generates defective MMMs. In the case of M_C^{Me}, where crosslinking only occurred in the PBI polymer regions, the chain packing in the polymer matrix might become denser hence creating larger gap at the interface of MOF and polymer. Consequently, defect formation in M_C^{Me} also resulted in a much higher acetone permeance (Figure 6f).

3. Conclusions

We demonstrated the successful development of a multizoning method for the fabrication of MMMs with seamless cross-sections and asymmetric-filler densities, where MOF nanoparticles were concentrated on the surface of the membrane. This methodology addresses the drawbacks of the conventional direct mixing method, which results in underutilization of MOF fillers owing to their even distribution across the membrane cross-section (interior). We demonstrated that concentrating MOF nanoparticles on the membrane surface is beneficial for nanofiltration applications, particularly in enhancing the solvent permeance while maintaining selectivity. The multizoning method allows to separately optimize the fillers and polymer characteristics, which provides the opportunity to combine limitless MOF–polymer pairs. Using polybenzimidazole polymer and Zr–BI–**fcu**-MOF, we demonstrated that MOF–polymer adhesion in MMMs can be improved by the appropriate selection of MOF and polymer pairs to enable a substantial MOF–polymer overlap at the interface, with preferential interactions between the polymer and the inner pore wall of the MOFs. This enables us to limit the dynamics of the polymer to achieve better control of the molecular sieving throughout the MOF accessible porosity. Furthermore, nanodomain analysis using nano-FTIR spectroscopy revealed for the first time that some parts of the MOF nanoparticles on the MMM surface were partially covered by the polymer matrix. The exposed part of the MOF surface allowed for direct interaction with the molecules to be separated and acting as channels for molecular transportation. Finally, we showed that crosslinking MMMs with distinct MOF linker functionalities enhanced the solvent stability and controlled the molecular sieving performance. Our design strategy is generally applicable to the fabrication of composite materials with seamless interface at the nanoscale and asymmetric-filler density at the macroscale.

4. Molecular Simulations

The cell parameters of the slab models are a = 33.331 Å, b = 47.137 Å, c = 104.259 Å, $\alpha = \beta = \gamma = 90°$ for Zr–Me–**fcu**-MOF and a = 33.331 Å, b = 47.137 Å, c = 100.000 Å, $\alpha = \beta = \gamma = 90°$ for Zr–BI–**fcu**-MOF optimized at DFT level by using the CP2K software package[44,45] leaving a vacuum region of 20 Å (see the Supporting Information for details). Zr atoms were capped by −OH groups, and the remaining H^+ formed an −OH group with a framework O atom at the surface,[46] and the partial charges are derived from the density-derived electrostatic and chemical (DDEC6) method as implemented in the CHARGEMOL module code.[47] Lennard–Jonnes parameters were extracted from DREIDING[48] and UFF force fields for the slab models and GAFF forcefield for the PBI polymer, se details in Tables S13 and S14 (Supporting Information). The polymer was constructed using Polymatic code[40] and the ESP partial charges of PBI were extracted from the central monomer of the trimeric system. The PBI configuration was generated from this initial model by performing a procedure containing 21 MD steps,[39,49] to reach an experimental density of 1.11 g cm^{-3} and the combination of polymer and composite also followed the 21-step classical MD scheme that integrated the NVT and NPT cycles using the LAMMPS.[41] The pore limiting diameter was calculated using the DFT optimized bulk structure a =

b = c = 33.331 Å, $\alpha = \beta = \gamma = 90°$ for both MOFs. Finally, the interaction energy was calculated by using a model system of a small fragment of both the Zr–Me–**fcu**-MOF and Zr–BI–**fcu**-MOF containing two inorganic clusters, their connecting linkers, and two PBI chains and we employed the B3LYP functional with the DGauss DGDZVP basis set.[50]

5. Experimental Section

*Synthesis of Zr–BI–**fcu**-MOF*: 4,4′-(1H-benzo[d]imidazole-4,7-diyl)dibenzoic acid (320 mg, 0.9 mmol) was dissolved in 30 mL dimethylformamide (DMF), and ZrCl$_4$ (210 mg, 0.9 mmol) was dissolved in a mixed solvent of 30 mL DMF and 3 mL trifluoroacetic acid (TFA). The two solutions were mixed and sealed in capped round-glass bottle. The mixture was maintained at 120 °C for 48 h under continuous stirring and then allowed to cool to room temperature. The MOF precipitates were separated by centrifugation, washed with dimethylacetamide (DMAc), and dispersed in DMAc to form a uniform suspension. 1 mL of the sample suspension in DMAc was collected, separated the sample by centrifugation, and washed the sample with acetone several times. After drying the sample in an oven at 150 °C overnight, the solid sample was weighed, and the yield of Zr–BI–**fcu**-MOF was calculated to be ≈80% based on the ligand.

*Synthesis of Zr–Me–**fcu**-MOF*: The synthesis of Zr–Me–**fcu**-MOF was the same as that of Zr–BI–**fcu**-MOF except that 2′,5′-dimethyl-[1,1′:4′,1′′-terphenyl]−4,4′′-dicarboxylic acid was used as a ligand instead of 4,4′-(1H-benzo[d]imidazole-4,7-diyl)dibenzoic acid.

MMM Fabrication: M^0 was prepared by casting a PBI film (made from 18 wt% in DMAc) on a porous nonwoven Novatexx 2471 polypropylene (PP) flat sheet with a casting thickness of 250 μm at a casting speed of 4 cm s^{-1} using a film applicator (Elcometer 4340). Subsequently, the formed film was immediately immersed in an acetonitrile coagulation bath at 23 °C for 24 h. Acetonitrile was used as the coagulation medium to preserve the crystallinity of the MOFs during MMM fabrication. M^{BI} was fabricated using the multizoning method. Before casting, two batches of the dope solutions were prepared. The first dope solution contained only PBI and DMAc in a weight ratio of 18:82. The second dope solution contained MOFs (Zr–BI–**fcu**-MOF), PBI polymer, and a DMAc solvent. In a typical procedure, a suspension of MOF particles (100 mg) in DMAc (1130 mg) and a PBI dope solution (770 mg; 26 wt% in DMAc) was blended using mechanical stirring under an inert atmosphere. The blend was then placed in a roller for 24 h to obtain a homogeneous solution. Bubbles were removed by incubation before casting. The final weight ratio of the polymer to MOF in the dope solution was 10:5 (Table S1, Supporting Information). To form the first wet film, the first batch of the dope solution was cast on the PP support using a film applicator (Elcometer 4340) with a casting knife thickness of 250 μm at a casting speed of 4 cm s^{-1}. Immediately after the first wet film was formed, the second dope solution was cast onto the first wet film with a casting knife thickness of 275 μm (leaving a 25 μm gap for the thickness of the second film) at a casting speed of 4 cm s^{-1}. The cast film was immediately immersed in an acetonitrile coagulation bath at 23 °C to form ISA MMMs. M$^{BI}_{DM}$ was fabricated using a conventional direct mixing approach. A dope solution containing Zr–BI–**fcu**-MOF (60 mg) in DMAc (863 mg) was blended with a PBI dope solution (2077 mg; 26 wt% in DMAc) using mechanical stirring under an inert atmosphere. The blend was then placed in a roller for 24 h to obtain a homogeneous solution. Bubbles were removed by incubation before casting. The final mass ratio of the polymer to the MOF in the dope solution was 18:2 (Table S1, Supporting Information). The doped solution was cast onto a porous nonwoven Novatexx 2471 PP using a film applicator (Elcometer 4340) with a casting knife thickness of 250 μm at a casting speed of 4 cm s^{-1}. The cast film was immediately immersed in an acetonitrile coagulation bath at 23 °C to form the membrane. M^{Me} was fabricated in the same way as M^{BI}, except that Zr–Me–**fcu**-MOF was used. M$^{BI}_C$ was fabricated in the same way as M^{BI} and was then crosslinked in 3 wt% DBX in acetonitrile solution at

**ADVANCED
SCIENCE NEWS**

www.advancedsciencenews.com

**ADVANCED
MATERIALS**

www.advmat.de

85 °C for 24 h. M_C^{Me} was fabricated in the same way as M^{Me}, and was then crosslinked in 3 wt% DBX in acetonitrile solution at 85 °C for 24 h.

MMM Optimizations: The optimization of the multizoning method is detailed in the Supporting Information under section "MMMs fabrication optimization" and shown in Figure S7 (Supporting Information). The dope solution concentration and the casting thickness was optimized.

X-Ray Diffraction (XRD) Analysis: The XRD data were collected using a Cu K$_\alpha$ Bruker D8 Advance diffractometer in the angular range that contained the peaks of interest: 2θ 3°–30° in steps of 0.02° and at a scanning speed of 10° min^{-1}. Before data collection, the samples were placed in a zero-background XRD sample holder.

Attenuated Total Reflectance Fourier Transform Infrared (ATR-FTIR) Spectroscopy Analysis: An FTIR-Nicolet iS10 spectrometer was used over the wavenumber range of 600–4000 cm^{-1} with 64 scans for each sample.

Nano-FTIR Analysis: Nano-FTIR spectroscopy (Neaspec GmbH) was performed using a laser centered at a wavenumber of ≈1300 cm^{-1}. A series of FTIR spectra were collected along a 3000 nm scanning line, which resulted in a spatial resolution of 30 nm. An AFM tip that was Pt/Ir-coated and had a frequency of 75 kHz was used. The membrane sample was attached to a silicon wafer by taping its edges with silver tape. A standard TGQ1 reference sample was used to optimize the signal from the instrument.

Scanning Electron Microscopy (SEM): A scanning electron microscope (Magellan) was used to examine the surface and cross-sectional morphologies of the top of the membrane. First, the membranes were dried at room temperature for 1 day. They were then placed in a vacuum oven at 25 °C for 1 day. The dried membranes were then peeled off the PP support and the fractures were used for cross-sectional analysis. The prepared membranes were attached to the SEM stub using carbon tape and then coated with 5 nm iridium using an ion sputtering device before SEM analysis. Images were acquired at 3 kV high tension and a current of 13 pA, with a working distance of 5 mm. To perform energy dispersive X-ray spectroscopy (EDX) analysis for elemental mapping of the membrane, a Teneo instrument was used at 15 kV high tension with a 40 nA current.

Nanofiltration Performance Testing: A cross-flow nanofiltration skid with an active area of 3 cm^2, a back-pressure regulator, high-pressure pump, and microannular gear pump were used for membrane separation. The flow rate of the microannular gear pump was maintained at a constant rate of 100 L h^{-1} to minimize concentration polarization. The membranes were conditioned in a solvent–solute mixture at 30 bars for 24 h before the permeate and retentate samples were collected to determine the rejection (Equation (1)). Polystyrene standards having 1 g L^{-1} PS580 and PS1300, 0.1 g L^{-1} methyl styrene dimer (236 g mol^{-1}), 10 μm dyes, and 10 μm active pharmaceutical ingredients (API) were used as solutes in the feed stream. The list of the tested solutes is provided in Table S3 (Supporting Information). The volume of solvent that permeated through the membrane (V) at a certain time (t) over the active membrane surface area (A) was used to calculate the flux (Equation (2)). The reported membrane performance values were the average values of three independently prepared membranes

$$\text{Rejection} \ (\%) = \left(1 - \frac{C_{permeate}}{C_{retentate}}\right) \times 100 \tag{1}$$

$$\text{Flux} \ (\text{L m}^{-2}\text{h}^{-1}) = \frac{V}{A.t} \tag{2}$$

Supporting Information

Supporting Information is available from the Wiley Online Library or from the author.

Acknowledgements

Conflict of Interest

The authors declare no conflicts of interest.

Author Contributions

R.H: conceptualization, methodology, MMM fabrication and characterizations, visualization, writing–review and editing. J.T.: MOF synthesis and characterization. D.F.: performed the DFT and force-field-based MD simulations of the 3D MOFs and their surface slab models. S.N.: performed the MD simulations on the PBI. A.D.M.: performed the MD simulations on the MMMs and analyzed the interfaces. O.S.: MOF synthesis and characterization, supervision, project discussions, writing, and editing. G.M.: supervised the overall molecular simulation works. M.E.: conceptualization, resources, methodology, writing–review & editing, supervision. G.S.: conceptualization, resources, methodology, writing–review & editing, supervision, funding acquisition, project administration.

Data Availability Statement

The data that support the findings of this study are available from the corresponding author upon reasonable request.

Keywords

[1] D. S. Sholl, R. P. Lively, *Nature* **2016**, *532*, 435.
[2] P. Marchetti, M. F. Jimenez Solomon, G. Szekely, A. G. Livingston, *Chem. Rev.* **2014**, *114*, 10735.
[3] S. Qiu, M. Xue, G. Zhu, *Chem. Soc. Rev.* **2014**, *43*, 6116.
[4] Y. Deng, Y. Wu, G. Chen, X. Zheng, M. Dai, C. Peng, *Chem. Eng. J.* **2021**, *405*, 127004.
[5] Q. Qian, P. A. Asinger, M. J. Lee, G. Han, K. Mizrahi Rodriguez, S. Lin, F. M. Benedetti, A. X. Wu, W. S. Chi, Z. P. Smith, *Chem. Rev.* **2020**, *120*, 8161.
[6] V. Chernikova, O. Shekhah, Y. Belmabkhout, M. Karunakaran, M. Eddaoudi, *Angew. Chem., Int. Ed.* **2023**, *62*, 202218842.
[7] A. R. Kamble, C. M. Patel, Z. V. P. Murthy, *Renewable Sustainable Energy Rev.* **2021**, *145*, 111062.
[8] B. Ghalei, K. Sakurai, Y. Kinoshita, K. Wakimoto, A. P. Isfahani, Q. Song, K. Doitomi, S. Furukawa, H. Hirao, H. Kusuda, S. Kitagawa, E. Sivaniah, *Nat. Energy* **2017**, *2*, 17086.
[9] Y. Tang, Y. Lin, D. M. Ford, X. Qian, M. R. Cervellere, P. C. Millett, X. Wang, *J. Membr. Sci.* **2021**, *640*, 119810.

[10] M. J. C. Ordoñez, K. J. Balkus, J. P. Ferraris, I. H. Musselman, *J. Membr. Sci.* **2010**, *361*, 28.

[11] J. Campbell, G. Székely, R. P. Davies, D. C. Braddock, A. G. Livingston, *J. Mater. Chem. A* **2014**, *2*, 9260.

[12] S. Sorribas, P. Gorgojo, C. Téllez, J. Coronas, A. G. Livingston, *J. Am. Chem. Soc.* **2013**, *135*, 15201.

[13] S. Xie, X. Zhang, X. Tan, W. Zhang, W. Guo, N. Han, Z. Zhou, Y. Jiang, I. F. J. Vankelecom, J. Fransaer, *ACS Mater. Lett.* **2022**, *4*, 1721.

[14] S. Zhou, Y. Wei, L. Zhuang, L-X. Ding, H. Wang, *J. Mater. Chem. A* **2017**, *5*, 1948.

[15] S. Zhou, O. Shekhah, J. Jia, J. Czaban-Jóźwiak, P. M. Bhatt, A. Ramírez, J. Gascon, M. Eddaoudi, *Nat. Energy* **2021**, *6*, 882.

[16] R. Hardian, Z. Liang, X. Zhang, G. Szekely, *Green Chem.* **2020**, *22*, 7521.

[17] Z. Huang, H. Guan, W. lee Tan, X-Y. Qiao, S. Kulprathipanja, *J. Membr. Sci.* **2006**, *276*, 260.

[18] F. Asvadi, A. Raisi, A. Aroujalian, *Microporous Mesoporous Mater.* **2017**, *251*, 135.

[19] M. S. Pacheco, G. E. Kano, L. de A. Paulo, P. S. Lopes, M. A. de Moraes, *Int. J. Biol. Macromol.* **2020**, *152*, 803.

[20] M. Benzaqui, R. Semino, N. Menguy, F. Carn, T. Kundu, J-M. Guigner, N. B. McKeown, K. J. Msayib, M. Carta, R. Malpass-Evans, C. L. Guillouzer, G. Clet, N. A. Ramsahye, C. Serre, G. Maurin, N. Steunou, *ACS Appl. Mater. Interfaces* **2016**, *8*, 27311.

[21] I-D. Carja, S. R. Tavares, O. Shekhah, A. Ozcan, R. Semino, V. S. Kale, M. Eddaoudi, G. Maurin, *ACS Appl. Mater. Interfaces* **2021**, *13*, 29041.

[22] N. Tien-Binh, H. Vinh-Thang, X. Y. Chen, D. Rodrigue, S. Kaliaguine, *J. Mater. Chem. A* **2015**, *3*, 15202.

[23] Y. Lee, C. Y. Chuah, J. Lee, T.-H. Bae, *J. Membr. Sci.* **2022**, *647*, 120309.

[24] L. Cseri, R. Hardian, S. Anan, H. Vovusha, U. Schwingenschlögl, P. M. Budd, K. Sada, K. Kokado, G. Szekely, *J. Mater. Chem. A* **2021**, *9*, 23793.

[25] A. Knebel, A. Bavykina, S. J. Datta, L. Sundermann, L. Garzon-Tovar, Y. Lebedev, S. Durini, R. Ahmad, S. M. Kozlov, G. Shterk, M. Karunakaran, I. D. Carja, D. Simic, I. Weilert, M. Klüppel, U. Giese, L. Cavallo, M. Rueping, M. Eddaoudi, J. Caro, J. Gascon, *Nat. Mater.* **2020**, *19*, 1346.

[26] Y. Cheng, B. Joarder, S. J. Datta, N. Alsadun, D. Poloneeva, D. Fan, R. Khairova, A. Bavykina, J. Jia, O. Shekhah, A. Shkurenko, G. Maurin, J. Gascon, M. Eddaoudi, *Adv. Mater.* **2023**, *35*, 2300296.

[27] Z. Wang, W. Wang, T. Zeng, D. Ma, P. Zhang, S. Zhao, L. Yang, X. Zou, G. Zhu, *Adv. Mater.* **2022**, *34*, 2104606.

[28] L. Xiang, L. Sheng, C. Wang, L. Zhang, Y. Pan, Y. Li, *Adv. Mater.* **2017**, *29*, 1606999.

[29] D. Fan, A. Ozcan, O. Shekhah, R. Semino, M. Eddaoudi, G. Maurin, *J. Membr. Sci. Lett.* **2022**, *2*, 100029.

[30] J. Jia, L. Gutiérrez-Arzaluz, O. Shekhah, N. Alsadun, J. Czaban-Jóźwiak, S. Zhou, O. M. Bakr, O. F. Mohammed, M. Eddaoudi, *J. Am. Chem. Soc.* **2020**, *142*, 8580.

[31] T. Xu, P. Zhang, F. Cui, J. Li, L. Kan, B. Tang, X. Zou, Y. Liu, G. Zhu, *Adv. Mater.* **2023**, *35*, 2204553.

[32] S. J. Datta, A. Mayoral, N. Murthy Srivatsa Bettahalli, P. M. Bhatt, M. Karunakaran, I. D. Carja, D. Fan, P. Graziane, M. Mileo, R. Semino, G. Maurin, O. Terasaki, M. Eddaoudi, *Science* **2022**, *376*, 1080.

[33] N. H. M. Nordin, A. F. Ismail, A. Mustafa, R. S. Murali, T. Matsuura, *RSC Adv.* **2014**, *4*, 52530.

[34] Ş. B. Tantekin-Ersolmaz, Ç. Atalay-Oral, M. Tatlıer, A. Erdem-Şenatalar, B. Schoeman, J. Sterte, *J. Membr. Sci.* **2000**, *175*, 285.

[35] J. Wang, G. Wang, Z. Zhang, G. Ouyang, Z. Hao, *RSC Adv.* **2021**, *11*, 36577.

[36] M. G. García, J. Marchese, N. A. Ochoa, *J. Appl. Polym. Sci.* **2010**, *118*, 2417.

[37] F. Huth, A. Govyadinov, S. Amarie, W. Nuansing, F. Keilmann, R. Hillenbrand, *Nano Lett.* **2012**, *12*, 3973.

[38] R. Hardian, P. Pogany, Y. M. Lee, G. Szekely, *J. Mater. Chem. A* **2021**, *9*, 14400.

[39] R. Semino, N. A. Ramsahye, A. Ghoufi, G. Maurin, *ACS Appl. Mater. Interfaces* **2016**, *8*, 809.

[40] L. J. Abbott, K. E. Hart, C. M. Colina, *Theor. Chem. Acc.* **2013**, *132*, 1334.

[41] A. P. Thompson, H. M. Aktulga, R. Berger, D. S. Bolintineanu, W. M. Brown, P. S. Crozier, P. J. in 't Veld, A. Kohlmeyer, S. G. Moore, T. D. Nguyen, R. Shan, M. J. Stevens, J. Tranchida, C. Trott, S. J. Plimpton, *Comput. Phys. Commun.* **2022**, *271*, 108171.

[42] I. B. Valtcheva, S. C. Kumbharkar, J. F. Kim, Y. Bhole, A. G. Livingston, *J. Membr. Sci.* **2014**, *457*, 62.

[43] M. A. Abdulhamid, R. Hardian, G. Szekely, *J. Membr. Sci.* **2021**, *638*, 119724.

[44] T. D. Kühne, M. Iannuzzi, M. Del Ben, V. V. Rybkin, P. Seewald, F. Stein, T. Laino, R. Z. Khaliullin, O. Schütt, F. Schiffmann, D. Golze, J. Wilhelm, S. Chulkov, M. H. Bani-Hashemian, V. Weber, U. Borštnik, M. Taillefumier, A. S. Jakobovits, A. Lazzaro, H. Pabst, T. Müller, R. Schade, M. Guidon, S. Andermatt, N. Holmberg, G. K. Schenter, A. Hehn, A. Bussy, F. Belleflamme, G. Tabacchi, et al., *J. Chem. Phys.* **2020**, *152*, 194103.

[45] J. Hutter, M. Iannuzzi, F. Schiffmann, J. VandeVondele, *WIREs Comput. Mol. Sci.* **2014**, *4*, 15.

[46] R. Semino, J. C. Moreton, N. A. Ramsahye, S. M. Cohen, G. Maurin, *Chem. Sci.* **2018**, *9*, 315.

[47] T. A. Manz, D. S. Sholl, *J. Chem. Theory Comput.* **2010**, *6*, 2455.

[48] S. L. Mayo, B. D. Olafson, W. A. Goddard, *J. Phys. Chem.* **1990**, *94*, 8897.

[49] D. Fan, A. Ozcan, N. A. Ramsahye, D. Zhao, G. Maurin, R. Semino, *ACS Mater. Lett.* **2021**, *3*, 344.

[50] N. Godbout, D. R. Salahub, J. Andzelm, E. Wimmer, *Can. J. Chem.* **1992**, *70*, 560.